Schaller, A., Streich, R., Drijkoningen, G., Ritter, O., Slob, E. (2018): A land-based controlled-source electromagnetic method for oil field exploration: An example from the Schoonebeek oil field. - *Geophysics*, *83*, 2, pp. WB1—WB17.

DOI: http://doi.org/10.1190/geo2017-0022.1

GEOPHYSICS, VOL. 83, NO. 2 (MARCH-APRIL 2018); P. WB1–WB17, 26 FIGS.
10.1190/GEO2017-0022.1

# A land-based controlled-source electromagnetic method for oil field exploration: An example from the Schoonebeek oil field

Andreas Schaller[1], Rita Streich[2], Guy Drijkoningen[1], Oliver Ritter[3], and Evert Slob[1]

## ABSTRACT

Controlled-source electromagnetic (CSEM) data are sensitive to the subsurface resistivity distribution, but 3D inversion results are ambiguous, and in-depth interpretation is challenging. Resolution and sensitivity analysis as well as the influence of noise on resolution have been used to quantify 3D inversion performance. Based on these numerical studies, a land-based CSEM survey was designed and carried out at the Schoonebeek oil field, the Netherlands. The acquired data were processed and subsequently inverted for the resistivity distribution. The 1D and 3D inversion of horizontal electric-field data show the reservoir at the right depth, matching well-log data without using a priori knowledge about the actual reservoir depth. We used a 1D model with fine layering as a starting model for 3D inversion. Synthetic data inversions and sensitivity tests demonstrate that resistive or conductive bodies inside the reservoir zone may be well-detectable with our limited acquisition geometry. Spatial variations in the reservoir resistivity are visible in the measured data and after inversion by assuming good knowledge of the background resistivity distribution. The reservoir resistivity and size, however, have to be interpreted with care considering the intrinsically low resolution of electromagnetic (EM) which is further reduced by manmade EM noise.

## INTRODUCTION

Since the first survey of an oil field offshore Angola using marine controlled-source electromagnetic (CSEM) sounding for determining the absence or presence of hydrocarbons in a known reservoir (Ellingsrud et al., 2002), the CSEM method has gained a lot of interest in the industry. The marine CSEM method is generally recognized to give additional information and is especially applied for hydrocarbon exploration, primarily with the objective to derisk drilling activities (Darnet et al., 2007; Constable, 2010; Fanavoll et al., 2014). Although in marine CSEM surveys, dense 2D profiles or complex 3D grids with tens of transmitter tow lines and hundreds to thousands of receiver deployments are feasible (Constable, 2010), such source and receiver coverage is very difficult to achieve for terrestrial surveys because of various logistical constraints (access restrictions, urbanization, presence of infrastructure, and noise sources) and typically limited equipment availability. In addition, deploying sources of sufficient strengths is difficult. In contrast to the marine case in which the transmitter is situated in the most conductive area, the seawater, land transmitters are usually situated on the earth's surface, and the source electrodes are deployed in a medium much more resistive than sea water, which limits achievable source current amplitudes. Furthermore, more near-surface heterogeneities exist on land than at the seafloor and near-electrode heterogeneities can result in more complex electric-field patterns.

Although electromagnetic (EM) methods were initially developed on land (Streich, 2016), the mentioned problems and challenges of land EM make it difficult to replicate the marine EM exploration success on land. To date, the seismic method is the principal geophysical method that is routinely applied for hydrocarbon exploration on land. Seismic wave-propagation method provides higher resolution than the diffusive CSEM method. However, CSEM methods have the advantage to be sensitive to resistive objects and to spatial variations in the resistivity. They provide generally higher resolution than potential-field methods such as gravity (Li and Oldenburg, 1998; Dell'Aversana et al., 2012). Large-scale EM surveys are not commonly carried out, but many wells exist with resistivity logs. Gathering additional EM data would provide knowl-

---

Manuscript received by the Editor 10 January 2017; revised manuscript received 23 August 2017; published ahead of production 13 November 2017; published online 28 December 2017.

[1] Delft University of Technology, Department of Geoscience and Engineering, Delft, The Netherlands. E-mail: A.M.Schaller@tudelft.nl; G.G.Drijkoningen@tudelft.nl.
[2] Shell Global Solutions International BV, Amsterdam, The Netherlands. E-mail: rita.streich@shell.com.
[3] GFZ German Research Centre for Geosciences, Potsdam, Germany. E-mail: oliver.ritter@gfz-potsdam.de.

edge of the resistivity distribution inside an oil or gas field, which is essential to evaluate its processes during hydrocarbon production or steam injection.

Numerical feasibility studies on land exist (Wirianto et al., 2010) and show that subsurface responses are weaker compared with marine CSEM responses and are more complicated to interpret due to near-surface inhomogeneities. Up to now, only a few academic EM surveys and a small number of industry surveys were conducted, which can be considered technology trials rather than commercial surveys (Streich and Becken, 2011; Grayver et al., 2014; Tietze et al., 2015; Streich, 2016). Grayver et al. (2014) showed that for a land CSEM survey, it is possible to get good 3D inversion results consistent with regional geology. They deployed 39 5C receivers along an 11 km long line centered at a $CO_2$ injection site and eight CSEM transmitters well distributed around the area. Several 3D inversion algorithms have been developed over the last decade to reconstruct resistivity models from marine and land EM data (Commer and Newman, 2008; Plessix and Mulder, 2008; Grayver et al., 2013; Oldenburg et al., 2013; Schwarzbach and Haber, 2013; Zhdanov et al., 2014). A recent review of the latest developments can be found in Newman (2014).

In this work, we study the applicability of land CSEM for recovering the resistivity distribution inside a hydrocarbon reservoir by 1D and 3D inversions. The underlying mathematical theory of EM inversion is well-established, but the practical application to real data requires thorough analysis of uncertainties in the inversion result. Therefore, we numerically investigate resolution capability in terms of the survey geometry, noise distortion, reservoir depth, and resistivity distribution inside the reservoir. We use a deterministic inversion approach, in which gradients derived from the forward-model process are used to update a sequence of models. Receivers are either inverted separately or together, and their inversion results are compared. Based on the results of the analysis, a target-oriented land CSEM acquisition field setup was designed for the Schoonebeek region in the Netherlands where steam is injected into an oil-bearing reservoir at a depth of approximately 700 m for enhanced oil recovery. The obtained data were inverted for the resistivity distribution inside the reservoir where the injected steam may lead to more complex resistivity patterns close to the injector and producer wells. We show how a sparse source-receiver configuration has the potential of resolving complex resistivity patterns inside the reservoir zone. Furthermore, we discuss to what extent small-scale variations of resistivity can be detected.

## INVERSION ALGORITHMS

### 1D inversion

We try to find a model for which we can compute data that will best fit the measured data. Finding this best-fitting model requires iterative (forward) modeling in which after every iteration, the model can be updated. This was done using a reflectivity forward modeling code (Streich and Becken, 2011; Streich et al., 2011). To minimize the number of iterations necessary to find the best-fitting model, we use a Gauss-Newton-type method to compute model updates based on an objective function that we seek to minimize. The objective function is given by

$$f_{1D} = \|\mathbf{W_d}(\mathbf{d} - F(\mathbf{m}))\|^2 + \mu\|\mathbf{W_m}(\partial_\mathbf{z}(\mathbf{m} - \mathbf{m_0}))\|^2, \quad (1)$$

where the first term is the misfit of the model's computed response $F(\mathbf{m})$ to the data $\mathbf{d}$ that are the real and imaginary parts of the measured electric-field data. The data vector $\mathbf{d}$ can contain data from multiple transmitters, receivers, and frequencies. The data weights are defined as $\mathbf{W_d} = \mathrm{diag}(w_i)$, where the weights $w_i$ are calculated by multiplying error estimates with the absolute value of the data. They weigh the relative contribution of each datum to the misfit. Data with large errors are down weighted to limit their influence, whereas data with small errors will have a larger impact on the total misfit. The second term is a norm of the model roughness and is computed by applying a differencing operator $\partial_\mathbf{z}$, a matrix of first derivatives with respect to depth, to the elements of the model vector $\mathbf{m}$, and $\mathbf{m_0}$ is a reference model, e.g., the starting model. We use a bounded logarithmic transform of the conductivity $\sigma_{h,v}$ to the model parameters (Grayver et al., 2013), where $\sigma_{h,v}$ represents horizontal and vertical conductivities. For the logarithmic transform, upper and lower conductivity bounds of $10^{-4}$ S/m (10,000 Ωm) and 1.5 S/m (2/3 Ωm) were used. The variable $\mathbf{W_m}$ is a diagonal weighting matrix that weighs the model variations and can consist of different measures of the model norm (Farquharson and Oldenburg, 1998); $\mu$ is a regularization parameter that weighs the data- and model-dependent terms of the objective function and contains a reduction exponent that gradually decreases the regularization ("cooling") at each iteration (Haber et al., 2000). The regularization parameter at iteration $n$ is computed as $\mu = (\mu_i)/(n+1)^p$ where the regularization parameter $\mu_i$ weighs the data- and model-dependent terms and $p$ is a parameter that defines by how much the influence of regularization is reduced at each iteration. For the modeling study, a simple least-squares weighting of the model variations $\mu_i = 0.05$ and $p = 1.67$ was used. By minimizing the first-order derivative of the conductivity depth profile in addition to minimize the data misfit, the regularization seeks to generate a smooth model. Although there is no physical argument in using a smoothing constraint, smooth models are less likely to result in over-interpretation of the data because they will not contain small-scale features that are poorly constrained by the data. Our algorithm is similar to the Occam inversion (Constable et al., 1987; deGroot Hedlin and Constable, 1990; Key, 2009), but it does not include a search for the optimum regularization parameter. We found that in most cases, field data cannot be fit to within a prescribed error level and searching for an adequate regularization parameter would return very small values of the objective function, leading to instable models. The algorithm is stable and rapidly convergent: A smoothed version of the true structure is typically recovered in 12–16 iterations.

The misfit $x_{\mathrm{rms}}$ is defined as the global root-mean-square (rms) error:

$$x_{\mathrm{rms}} = \frac{1}{n}\sqrt{\sum_{i=1}^{n} W_{d_i}[d_i - F_i(\mathbf{m})]^2}, \quad (2)$$

where $n$ is the number of data points. The inversion is terminated if the target rms is reached or if either the objective function or the rms cannot be reduced during several subsequent iterations.

### 3D inversion

The forward modeling algorithm used in the 3D inversion code consists of solving the second-order partial differential equations (Mulder, 2006; Plessix et al., 2007):

$$i\omega\mu_0\bar{\sigma}\mathbf{E} - \nabla \times \nabla \times \mathbf{E} = -i\omega\mu_0\mathbf{J}_\mathbf{s} \tag{3}$$

where $\mathbf{E}(\omega, \mathbf{x})$ represents the electric-field components as a function of angular frequency $\omega$ and position $\mathbf{x}$, the complex conductivity $\bar{\sigma} = \sigma + i\omega\epsilon$ includes conductivity $\sigma(\mathbf{x})$ and electric permittivity $\epsilon$, and $\mu_0$ is the magnetic permeability; $\mu$ and $\epsilon$ are assumed to be constant at their free-space values. We do not consider frequency-dependent conductivity variations; induced polarization effects are irrelevant for the fairly resistive geologic settings studied here. The current source is $\mathbf{J}_\mathbf{s}(\omega, \mathbf{x})$. Equation 3 is discretized using a finite-volume-type discretization scheme resulting in a linear system of the form $\mathbf{AE} = \mathbf{F}$, where $\mathbf{A}$ is the discretized Maxwell operator, $\mathbf{E}$ represents the vector of the electric-field components on the discretized model, and $\mathbf{F}$ is the source vector. A conjugate-gradient iterative scheme, the BiCGStab2 scheme, preconditioned by a multigrid solver (Mulder, 2006) is used to solve the large and sparse, but symmetric and non-Hermitian, matrix $\mathbf{A}$. For multifrequency, multisource CSEM modeling, the code is parallelized over sources and frequencies. For further details of the forward-modeling engine, the reader is referred to Plessix et al., (2007).

The inverse problem seeks to find a conductivity model that minimizes the weighted least-squares functional:

$$f_{3D} = \frac{1}{2}\|\mathbf{W_d}(\mathbf{d} - F(\mathbf{m}))\|^2 + R. \tag{4}$$

The value of $F(\mathbf{m})$ is obtained by solving equation 3, and $\mathbf{d}$ contains the electric-field data. To balance the update of the shallow and deeper parts, a model weighting scheme that mainly depends on depth is used (Plessix and Mulder, 2008). We invert for the logarithm of the conductivity and impose upper and lower hard conductivity bounds. The data weights $\mathbf{W_d}$ are computed from the data amplitudes and noise; $R$ is a regularization term given by $R = \sum \alpha_n(|\mathbf{m} - \mathbf{m}_0|^2)$, where $n$ are the spatial directions and $\alpha_n$ are positive numbers that are calibrated such that the magnitude of the regularization term remains a small fraction of the total objective function value throughout the inversion. The objective function is then solved by using a quasi-Newton method, the limited-memory BFGS method (Byrd et al., 1995), and a box average filter is applied to the gradient of the objective function to smooth the spatially rapid variations and geometry imprints arising from the sparse source and receiver spacing or fine model discretization. For computational efficiency, we terminated all inversions after a maximum of 25 iterations, when in most cases, convergence had slowed down, and we were not expecting further significant model updates and misfit reductions.

In the following, vertical transverse isotropic (VTI) inversions were carried out for 1D and 3D inversion using horizontal electric-field components $E_x$ and $E_y$ under the assumption that horizontal and vertical resistivities are different. If not mentioned explicitly, we focus on the vertical and do not show the horizontal resistivity because the inversion is more sensitive to the vertical resistivity inside the resistive reservoirs of interest.

## SYNTHETIC 3D RESOLUTION TESTS

### Resolution and sensitivity analysis

The Schoonebeek reservoir layer is located at approximately 700–800 m depth, and its structure is well-known from well logs, 3D seismic data, and production data. We found from forward modeling tests that the strongest reservoir responses should be obtained, while maintaining acceptable signal amplitudes, at source-receiver offsets between approximately 3 and 5 km.

The detailed numerical resolution and sensitivity analysis were carried out based on known properties of the Schoonebeek oil field in the Netherlands with the objective of obtaining high resolution toward a resistive reservoir target zone.

Resolution is the measure for the distance that two separated objects should have, to be identified as two objects and not as one single object. Thus, two objects can be resolved when their separation is larger than the minimum separation distance and their contrast to the background is higher than a predefined value. An object is detectable when amplitude differences of data with and without this object are sufficiently large and the phase differences are above the detection limit. An object can therefore be detectable but not resolvable.

We modeled a range of complex structures inside the Schoonebeek reservoir target zone to understand (1) the minimum size of a feature that is still detectable taking into account a specific acquisition geometry limited by various logistical constraints and (2) resolution limits and the capability to recover resistivity values.

To minimize the impact and cost of the survey, we aim for a sparse field setup with few source locations and a small number of receivers. Synthetic sources and receivers were placed at positions where actual field deployment is possible such that the survey covers one of the locations where steam is being injected into the reservoir (Figure 1). The source available for our survey was a transmitter that feeds currents with a fixed phase relationship into three grounded electrodes. The overall source polarization can be adjusted by applying a constant phase shift to the three source currents (see Appendix A). We refer to this phase shift as the source polarization angle. Notice that the actual spatial orientation of the source polarization is determined by the combination of source geometry and the polarization angle applied. For the following synthetic calculations, if not mentioned otherwise, we modeled data for two transmitter positions and 15 receivers using source polarization angles of −30°, 30°, and 270°.

For forward modeling tests and as a background model for our 3D studies, we use a 1D background resistivity model that was obtained by taking the shallow subsurface resistivity information for the top 150 m from regional well-log data and resistivity at greater depths from 1D real-data CSEM inversion results of the Schoonebeek region (Figure 2). We tried a range of other starting models, but they gave poor convergence of the 3D inversion for field data, and thus, we limit our study to the mentioned background model.

In Figure 3, we display examples of data $d_1$ calculated for the model shown in Figure 2, and data $d_2$ for a model containing a

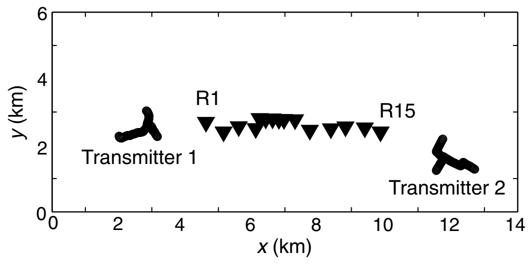

Figure 1. Source and receiver positions used for synthetic studies and field example.

resistive block, consistent with well-log resistivities of oil-saturated parts of the reservoir, at depths of 785–800 m. The obtained electric-field amplitudes and phases for both models are shown in Figure 3a–3d for 12 frequency values per receiver. The normalized amplitudes of the differences calculated as $|(d_2 - d_1/d_1) \times 100|$ are plotted in Figure 3e and 3f and their phase differences in degrees calculated as $|\arg(d_2)| - |\arg(d_1)|$ are plotted in Figure 3g and 3h. For increasing offsets, the sensitivity toward the resistive body inside the reservoir increases, whereas the overall amplitudes decrease by about two orders of magnitude. Furthermore, the largest differences occur at frequencies of approximately 1 Hz for the electric-field component $E_y$. Even though the largest differences occur near the minima of the electric field, the signal-to-noise ratio (S/N) for a typical noise-floor estimate of $10^{-10}$ V/m (Tietze et al., 2015), is still well greater than 1. Assuming a threshold of approximately 2° for a detectable phase difference and a threshold of approximately 5% for a detectable amplitude difference, then the modeled differences in the north–south component $E_x$ are too small to be detectable. Differences in the east–west component $E_y$ are sufficient for frequencies between 0.1 and 1 Hz and for source-receiver offsets larger than approximately 3.5 km. These results are important when considering appropriate survey geometry and frequency layout for real data collection.

To be able to resolve resistive or conductive structures at the reservoir depth, the survey geometry has to be chosen such that the sensitivity to this depth range is sufficiently high. We first calculated the cumulative sensitivity as a weighted $\ell^2$-norm resulting in a single sensitivity value for each model parameter that includes sensitivities with respect to all data values:

$$C(m_i) = \left( \sum_{j=1}^{n} \left| W_{d_j} \frac{\partial F_j(m)}{\partial m_i} \right|^2 \right)^{\frac{1}{2}}, \tag{5}$$

where $n$ is the number of data points counted over sources, source polarizations, receivers, and frequencies, $F_j(m)$ is the EM field at data point $j$, $(\partial F_j(m))/(\partial m_i)$ is the Fréchet derivative of the data with respect to the model parameter $m_i$, $W_{d_j} = 1/(F_j(m) + \epsilon)$ are data weights with $j = 1, \ldots, n$, and the absolute error floor is $\epsilon = 10^{-10}$ V/m. The cumulative sensitivities are normalized by their maximum value.

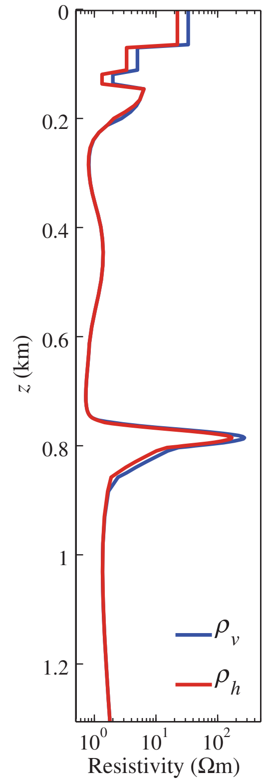

Figure 2. The 1D horizontal and vertical resistivity profile obtained from 1D CSEM inversion results of the Schoonebeek region and well log data and used as background model for 3D synthetic inversions.

Horizontal and vertical sensitivity sections for the 1D resistivity profile from Figure 2 and the survey geometry from Figure 1 are depicted in Figure 4. In Figure 4a, the logarithm of the normalized cumulative sensitivity to vertical resistivity at a depth level of 785 m is plotted, showing a high-sensitivity region between both transmitters and within an approximately 2 km wide corridor around the receiver locations, indicating that structures close to the receiver line should be detectable. Figure 4b shows the logarithm of normalized cumulative sensitivity in a vertical plane along the receiver line computed for the same conductivity model and survey geometry. The sensitivity is highest around the target depth of approximately 750 m. The sensitivity to the reservoir is high because of its high overall resistivity.

3D inversion solutions, especially for surveys with limited amounts of data and a sparse source-receiver configuration, are highly nonunique. Every solution depends on the regularization and inversion parameters chosen. To test data distribution and the inversion algorithm for the ability to recover a known structure using a limited survey geometry, we inverted two synthetic data sets created from two different model scenarios. Resistive and conductive bodies with certain dimensions were inserted into the reservoir layer to simulate a possible scenario of local resistivity variation due to steam injection. Again, the 1D resistivity profile shown in Figure 2 was used as a background model. In the first scenario, one large block with dimensions of $5000 \times 2000 \times 18$ m and horizontal and vertical resistivities $\rho_h = 200$ and $\rho_v = 333$ Ωm, respectively, was inserted into the reservoir (Figure 5a). In the second scenario, we inserted two somewhat smaller blocks, horizontally separated by 1 km. The block dimensions and resistivities were $2500 \times 2000 \times 18$ m; $\rho_h = 200$ Ωm, $\rho_v = 333$ Ωm and $1500 \times 2000 \times 18$ m; $\rho_h = 20$ Ωm, $\rho_v = 33$ Ωm (Figure 5b). We computed data for these two models with the source and receiver geometry shown in Figure 1. The inversion domain contains $201 \times 208 \times 142$ cells with lateral dimensions of $100 \times 100$ m and variable thicknesses, whereas automatic frequency-dependent regridding (Plessix et al., 2007) is used to reduce the computational cost for forward modeling and gradient calculations. One inversion run requires approximately 40 GB of memory and takes approximately 24 h to complete the 25 iterations. Assuming that we have good knowledge about the background resistivity, we start the 3D inversion from the 1D model result of Figure 2. Figure 5c and 5d shows depth slices inside the reservoir at a 785 m depth for an inversion result after 25 iterations for the single-block and double-block model scenarios. The boundaries of the objects after inversion, indicated by the dashed black lines, were in the following defined such that they coincide with a resistivity change of 10% from the background resistivity. Both inversions (Figure 5c–5f)

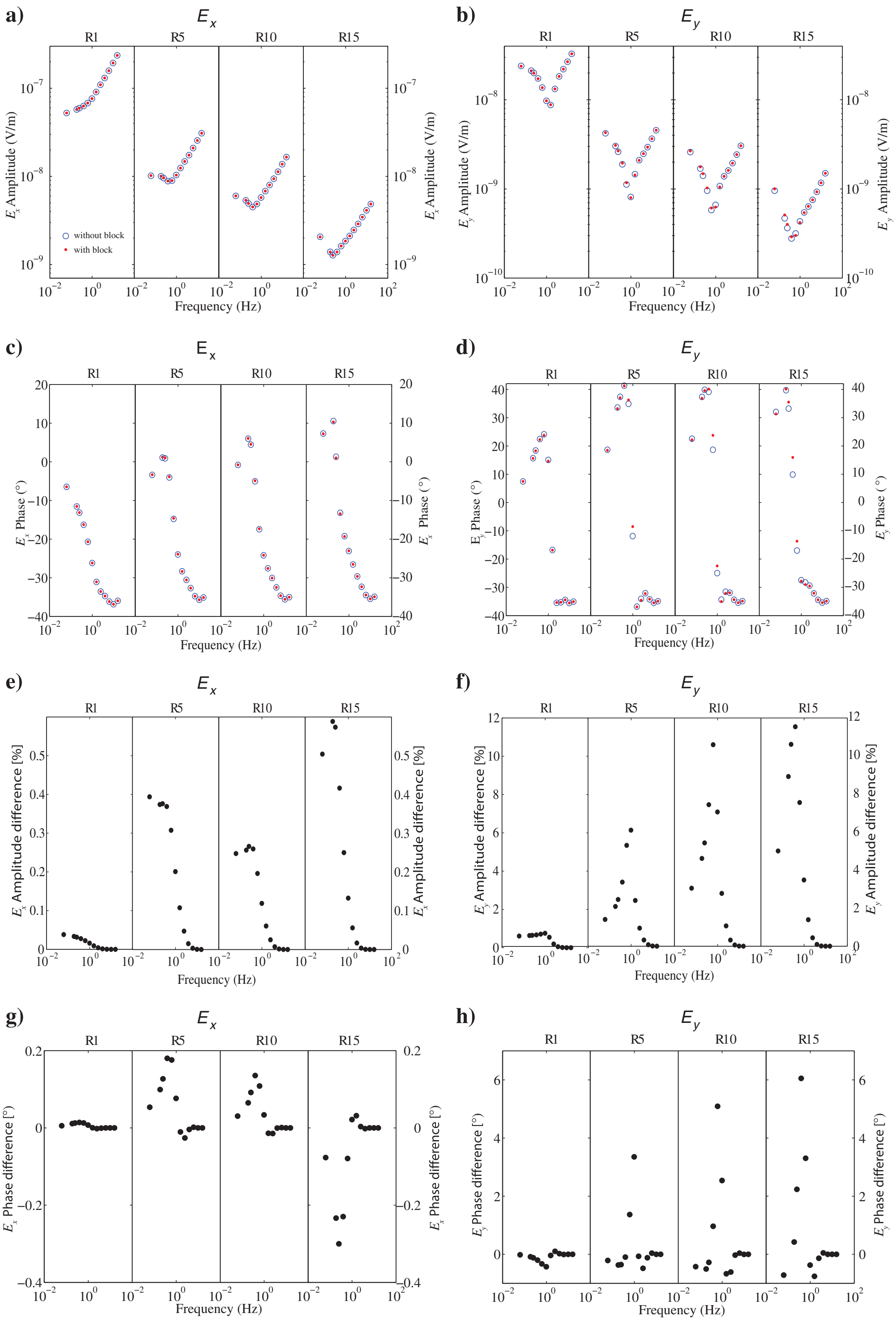

Figure 3. Electric-field data for transmitter 1 and for receiver position R1, R5, R10, and R15 with a source polarization angle of 30°. Electric-field amplitudes for (a) the north–south component $E_x$ and (b) the east–west component $E_y$ for the model shown in Figure 2 in blue and for the same Schoonebeek model with a block of dimensions $5000 \times 2000 \times 18$ m and a horizontal and vertical resistivity of 200 and 333 Ωm, respectively, added inside the reservoir in red, (c and d) the phase behavior, (e and f) the amplitude of the difference between the model with and without the resistive body in %, and (g and h) show the difference in phase.

detect the bodies and can resolve the bodies in resistivity and location, although the vertical and lateral extents of the bodies are slightly larger than their true extent. The vertical resolution for both modeled scenarios is high (Figure 5e and 5f). Most likely, the high resistivity of the background model and associated high sensitivity at the reservoir depth has helped focusing the images. The acquisition design is thus capable of resolving large conductive and resistive structures at the reservoir depth.

To further evaluate the 3D inversion performance of the acquisition design, we tested its ability to resolve small and complex structures (Figure 6). Two scenarios are discussed: two highly resistive bodies of $1 \times 1$ km separated by 500 m with $\rho_v = 1000\ \Omega\text{m}$, $\rho_h = \rho_v/2$ (Figure 6a) and a complex model with two highly resistive blocks and two blocks more conductive than the background reservoir and of different shapes with $\rho_{v,1} = 1000\ \Omega\text{m}$, $\rho_{v,2} = 100\ \Omega\text{m}$, and $\rho_h = \rho_v/2$ (Figure 6b). Figure 6c and 6d shows the inversion results at a depth of 785 m, and Figure 6e and 6f shows the inversion results for a vertical section in the depth range of the reservoir layer, whereas Figure 5 shows absolute resistivities and Figure 6 focuses on model updates. The anomalies with a small separation are difficult to resolve. This is illustrated by the resistivity profile along the black line in Figure 6c and by the dashed black line indicating the border of the resolved body with a resistivity increase of at least 10%. The two blocks are too close to each other to obtain two separate resistivity maxima. The complex scenario with four bodies can hardly be resolved horizontally and vertically assuming that amplitude differences lower than 10% are considered not to be detectable. Both inversions terminate before reaching the true resistivity values. Additional receivers perpendicular to the receiver line and two additional sources north and south of the receiver line were tested, but adding receivers hardly improved the resolution. Two additional sources, however, resulted in improved resolution for those bodies placed outside the receiver plane. Unfortunately, it is logistically impossible to add such sources in the field survey area. But because our primary interest is to resolve structures close to and underneath the receiver line, where we have resolution, the lack of resolution further away from the receiver plane is not of great concern.

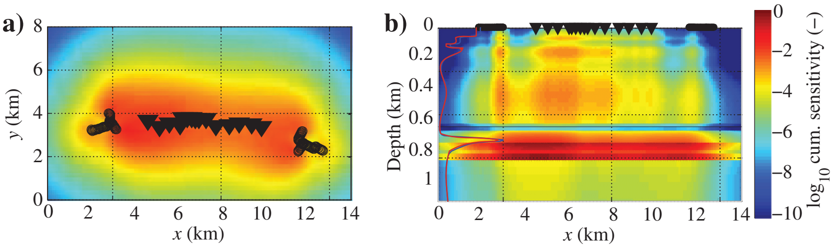

Figure 4. (a) Depth slice at reservoir level (785 m) of the normalized cumulative sensitivity to vertical resistivity. (b) Depth section of normalized cumulative sensitivity at $y = 4$ km. The black lines indicate the positions of the sources, and the black triangles indicate the positions of the receivers. As a reference, the 1D horizontal and vertical resistivity profile of Figure 2 is plotted on the left.

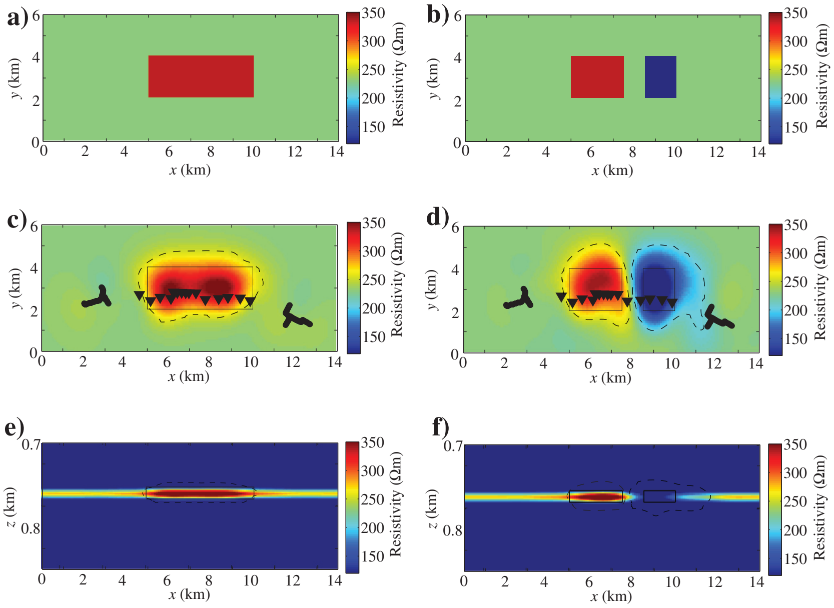

Figure 5. Inversion results after 25 iterations using the starting model shown in Figure 2 as the background model. (a) One-block scenario, (b) two-block scenario, and (c and d) the corresponding inversion results. Depth slices at reservoir depth of 785 m are shown in (a-d), whereas (e and f) the depth section around the reservoir. The black triangles are the receiver positions, and the black circles highlight the transmitter locations projected onto the depth slice. The black rectangles indicate the borders of the inserted bodies and the dashed black lines indicate the borders of the inserted bodies after inversion. Note that a linear scale for resistivity was applied.

## Choice of source polarization

To study the influence of source polarization on the quality of the inversion result, we analyzed synthetic data for single polarizations. Figure 7 displays 3D inversion results of three different polarizations of 30°, −30°, and 270° using data for transmitter 1, not considering transmitter 2. The dashed black lines indicate the borders of the resistive block after inversion. Only for a polarization of 270°, the resistivity and location of the resistive body are recovered accurately (the easternmost part cannot be recovered because of poor coverage), whereas its shape and amplitude are distorted when using source polarizations of 30° or −30°. To achieve better resolution, a range of preferably independent source polarizations can be used and inverted together (Figure 7d) because dependent polarizations in the data may deteriorate the inversion results (Grayver et al., 2014).

## Influence of noise on 3D inversion

A major aspect that influences the resolution is manmade EM noise. To assess the impact of field noise on resolution, uncertainties estimated from real data were used on synthetic data by applying weights to the data during the 3D inversion based on uncertainty information. An example of synthetic data with assigned uncertainties is shown in Figure 8, and inversion results are displayed in Figure 9. During inversion, data points with low S/Ns are down weighted, whereas data points with high S/Ns are up weighted to avoid significant model updates in regions where data misfits are high due to poor data quality. Estimated S/Ns of the real data were up to 65 dB. Data points for which the real data had estimated errors larger than 10% (i.e., an S/N of less than 20 dB) were neglected. These synthetic inversion results can be compared with the results obtained from noise-free synthetic data (Figure 6c and 6d), where the data weights were computed based on data amplitude only, not considering uncertainty information. The objective functions were reduced to approximately 3% (Figure 9a) and 4% (Figure 9b) of their initial values for the noise-free and the noisy scenarios. Using realistic data uncertainties, results in similar misfits but the shapes of the resolved bodies differ slightly, and the obtained resistivity updates for both scenarios are by approximately 3% less when compared with the noise-free scenarios. The rms values (Figure 9e) are low because we have used error estimates from field data, whereas our synthetic observed data are noise free and thus have lower error levels than the field data. Internal rescaling in our inversion makes absolute error levels practically insignificant. However, by using these error estimates, we modify relative weights of the data (down weight low-quality and up weight high-quality data points). These tests demonstrate that this slightly reduces the detectability of target structures.

### Summary

We have shown that CSEM data from a survey consisting of a single receiver line of 15 receivers with a length of approximately 6 km and two transmitters approximately inline with the receiver positions are sensitive to and capable to resolve a resistivity distribution inside a reservoir within a roughly 2 km wide corridor around the receiver plane. This setup further allows resolving resistive and conductive features introduced by injected fluids. Although resistive bodies can be recognized and located if the background resistivity distribution is well-known beforehand, their spatial dimensions and absolute resistivity cannot be resolved accurately, especially for small bodies inside the reservoir. The bodies are smeared out by the inversion, and the obtained resistivities are lower than the true values. The survey geometry used caused some decrease in resolution away from the receiver line and stronger smoothing of complex structures. Additional sources at positions perpendicular to the receiver line would have resulted in improved resolution of the 3D bodies. For the 3D inversion, a 1D starting model resembling the true resistivity structure is advantageous. Such a background model can be derived from 1D inversion results, well-log, and geologic information.

## FIELD EXAMPLE AT SCHOONEBEEK

The actual CSEM field survey experiment was carried out at the Schoonebeek oil field in the Netherlands in 2014 with focus on an area where steam is injected into a reservoir for enhanced oil recovery (Michou et al., 2013). The reservoir, which underwent major changes due to a 50 year production history (Rondeel et al., 1996), is located at a depth of approximately 700 m near the center of the receiver line and deepens to more than 800 m toward both transmitter locations. Source and receiver locations, as discussed in the modeling studies above, were used.

### Survey design

Given the limited accessibility (i.e., the border to Germany in the south and the town of Schoonebeek in the north) and economic considerations, our acquisition setup was limited to two sources at each end of the receiver line. Our modeling study showed that adding more receivers perpendicular to the receiver array did not improve the resolution. Figure 10 shows the geometry of the CSEM survey. There are 15 receivers at the surface spaced at roughly 0.5 km, with a denser spacing of 0.2 km toward the central part of the line. At 11 stations, only the horizontal electric-field components $E_x$ (north–south oriented) and $E_y$ (east–west oriented) were measured. At four stations, the three magnetic-field components were measured by deploying induction coils in all three spatial directions. The recording system used was the short-period automatic magnetotelluric (S.P.A.M. Mk. IV) data acquisition instrument developed by the German Research Centre for Geosciences (GFZ) (Klose et al.,

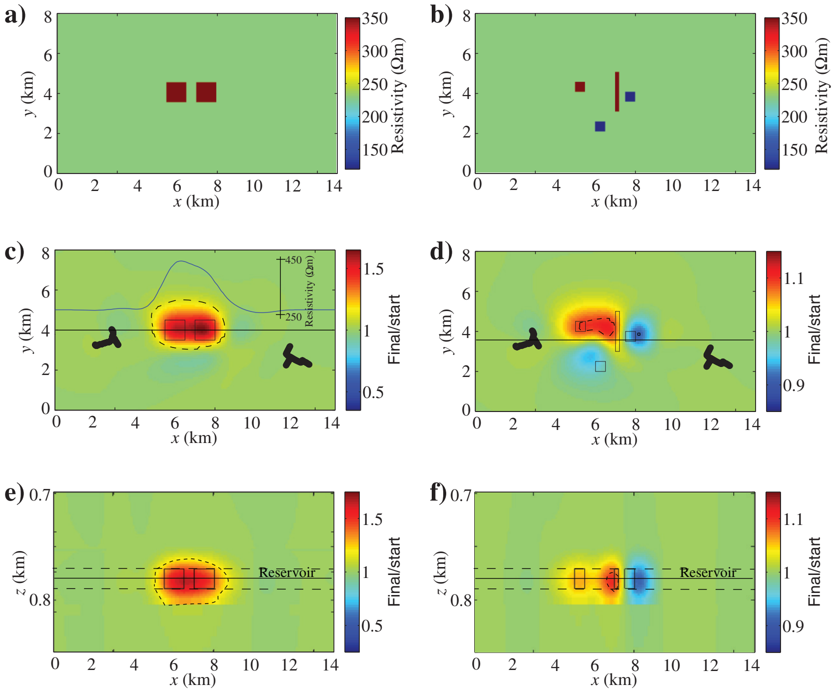

Figure 6. (a and b) Three-dimensional inversion results of the models. (c and d) Depth slices at reservoir depth of 785 m, and (e and f) the depth section around the reservoir. The solid black lines in (c and d) show the vertical cross section plotted in (e and f) and the solid black lines in (e and f) show the depth level of the depth slices plotted in (c and d). The black rectangles indicate the borders of the inserted bodies, and the black dashed lines indicate the borders of the inserted bodies after inversion.

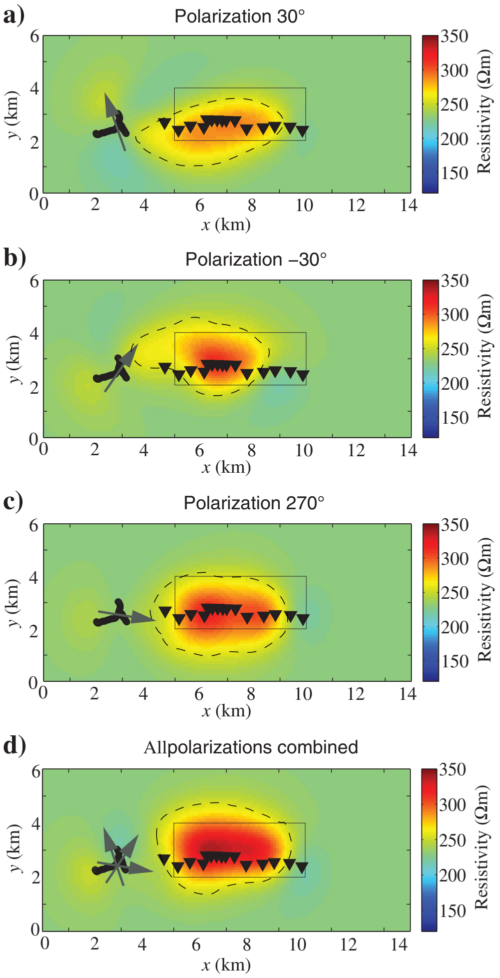

Figure 7. Dependence of the 3D inversion result on source polarization. Three different source polarizations are shown (see Appendix A): (a) 30°, (b) −30°, (c) 270°, and (d) all source polarizations combined. The synthetic 1 block model from Figure 5a was used for this study. The gray arrows indicate the approximate dipole orientation of the source signal.

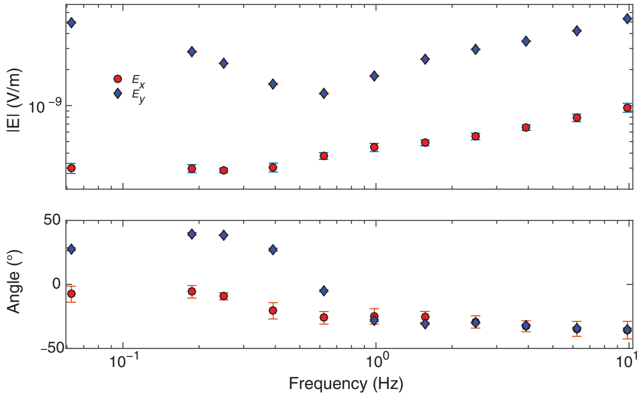

Figure 8. Example of synthetic data with error estimates from field data assigned. Data are for the two-block model from Figure 6a, transmitter 1 with polarization 270°, and receiver 11 (see Figure 1).

2011). The CSEM source is a horizontal electric dipole source that generates horizontal and vertical current flow in the subsurface. It has the ability to generate multiple current polarizations without physically moving the source, as explained above and in Appendix A. The transmitter locations east and west of the receivers were chosen such that the transmitter cables could be laid out along vehicle-accessible tracks in approximately T-shaped geometries resulting in approximately uniform azimuthal distribution of the CSEM source fields. To acquire useful CSEM data with sufficiently high S/Ns, we transmitted square-wave signals at different base frequencies. We transmitted periods of 16, 8, 4, 2, and 0.5 s to sample the entire frequency band that gives us information on the reservoir. At each position, the source transmitted currents with amplitudes up to approximately 38 A at 560 V for 15–20 h. We generated different source polarizations (−30°, 30°, 90°, and 270°) at Schoonebeek by adjusting the angle $\phi$ in equation A-1. For more details of the source properties, the reader is referred to Streich et al. (2013).

In the following, we only show electric-field data although we used magnetic-field data for quality control.

## Data processing

The data were processed to obtain response functions between the source and receivers. Some preprocessing was applied to improve S/Ns. First, a notch filter was applied to remove the 50 Hz signal and associated odd harmonics, followed by a high-pass filter to remove signals at frequencies lower than the primary source frequency. All time-domain receiver and transmitter data are processed using identical filter parameters. Subsequently, the data were split into short-time windows and transformed to and stacked in the frequency domain to effectively remove time-variable noise. In calculating response functions, data from different source periods and polarizations were combined. The calculation effectively deconvolved the source currents while not accounting for the source geometry or length of source wires. Bivariate response functions were obtained by choosing two of the three measured source currents fed into the three source electrodes (the third one is linearly dependent, yet the choice of currents may influence response function quality due to the noise characteristics of the data) according to equation B-3. To reduce the influence of noise, we use a robust processing scheme, a technique routinely used for magnetotelluric (MT) processing (Egbert and Booker, 1986; Chave and Thomson, 1989; Ritter et al., 1998; Streich et al., 2013). Obtained uncertainty estimates are used for automated data preselection and weighting during inversion. In addition, data with errors higher than 10% of the amplitudes were neglected. A more detailed description can be found in Appendix B.

Response functions for transmitter location 1 and for $E_x$ and $E_y$ are plotted in Figures 11 and 12. Figure 11 shows the response functions $T_{1,2}^{E_x}$, which is the horizontal electric-field component $E_x$, deconvolved from the source waveform, for the source polarized such that currents only flow through source electrodes 1 and 2, whereas the current on electrode 3 is zero. Figure 12 shows the response functions $T_{2,3}^{E_y}$ for $E_y$ and the source polarized such that only currents $I_2$ and $I_3$ flow through source electrodes 2 and 3, whereas the current $I_1$ on electrode 1 is zero. The amplitude and phase changes of the response functions $T_{1,2}^{E_x}$ (Figure 11) and $T_{2,3}^{E_y}$ (Figure 12) are smooth over the frequency spectrum of 1/16 to 100 Hz as well as between neighboring stations; this is to be expected from the diffusive nature of EM fields. Furthermore, amplitudes decay with distance from the source. The closest receiver, station R1 in Figure 11, however, shows much higher amplitudes and different phase characteristics on the $E_x$-component. These data, strongly influenced by near-source effects, could not be fitted by the inversion. Low S/Ns are a strong limitation to the measurements at Schoonebeek due to abundant EM noise sources. Attempts at quantifying ambient noise levels were made prior to the first CSEM survey. Noise levels were found to be strongly time variant (e.g., related to activities on nearby drill pads). Specific noise sources were identified as being nearby production sites, a pipeline running approximately north–south between receivers R6 and R7, and common urban infrastructure. Station R5 suffered from anomalous responses, strongly different from those recorded at the neighboring stations, possibly related to a nearby dairy factory or a well casing located less than 100 m from the receiver. Station R15 suffered from strong noise, likely related to very nearby production facilities. Because we did not succeed in removing this noise, stations R1, R5, and R15 would prevent the inversions of the entire data set from progressing and thus could not be considered. Numerous well steel casings present in the survey area are very likely to influence the measurements but are difficult to quantify numerically and are therefore not considered at this time.

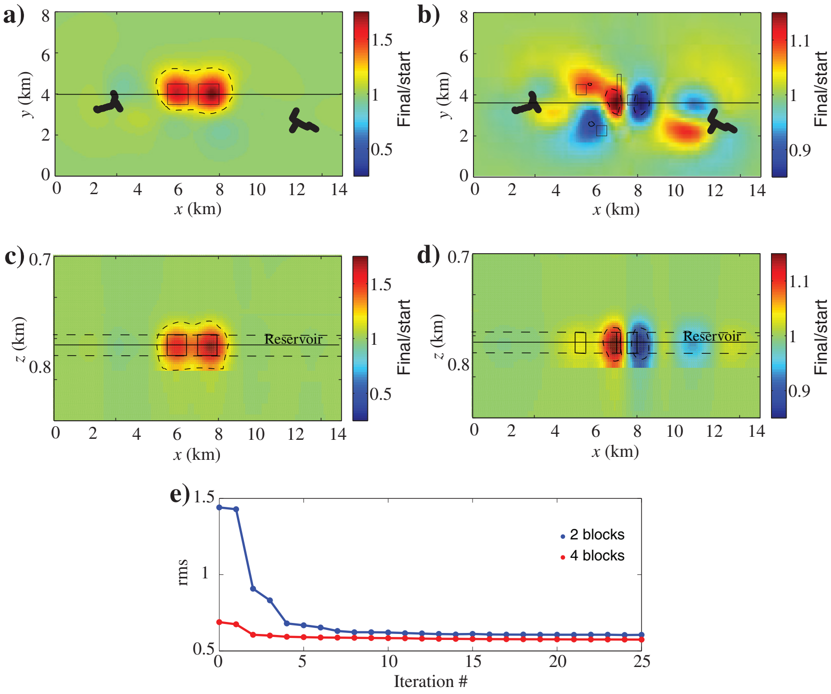

Figure 9. Influence of data uncertainties on inversion result. Data uncertainties obtained during processing are used as noise estimates. Inversion results for the model of Figure 6a are shown in a) and c), and inversion results for the model of Figure 6b are shown in (b and d). (a and b) show depth slices at reservoir depth of 785 m and (c and d) show the depth section around the reservoir. (e) The rms data misfits achieved. The noise-free scenarios are depicted in Figure 6c–6f, respectively.

## 1D inversion

We first invert our data (see Figures 11 and 12) for the resistivity distribution assuming a horizontally layered earth. The aim of the 1D inversion is to obtain a plausible starting model for a 3D inversion. Single-receiver and multireceiver inversions with joint sources were carried out for our 2C receivers. For a single-receiver inversion, the inversion was carried out separately for every source–receiver pair. Transmitted signals with different polarizations but the same source location are inverted together. For multireceiver inversions, the entire data set is inverted jointly resulting in one average resistivity model of the subsurface. The number of layers was set to 83 where layer thicknesses were allowed to vary with depth. To resolve the thin reservoir and its known high resistivity compared with its surroundings, layer thicknesses around the reservoir level were set to 2 m. The resistivity anisotropy ($\rho_v/\rho_h$) was constrained toward a ratio of 1.2, based on geologic information and inversion parameter testing. A regularization parameter

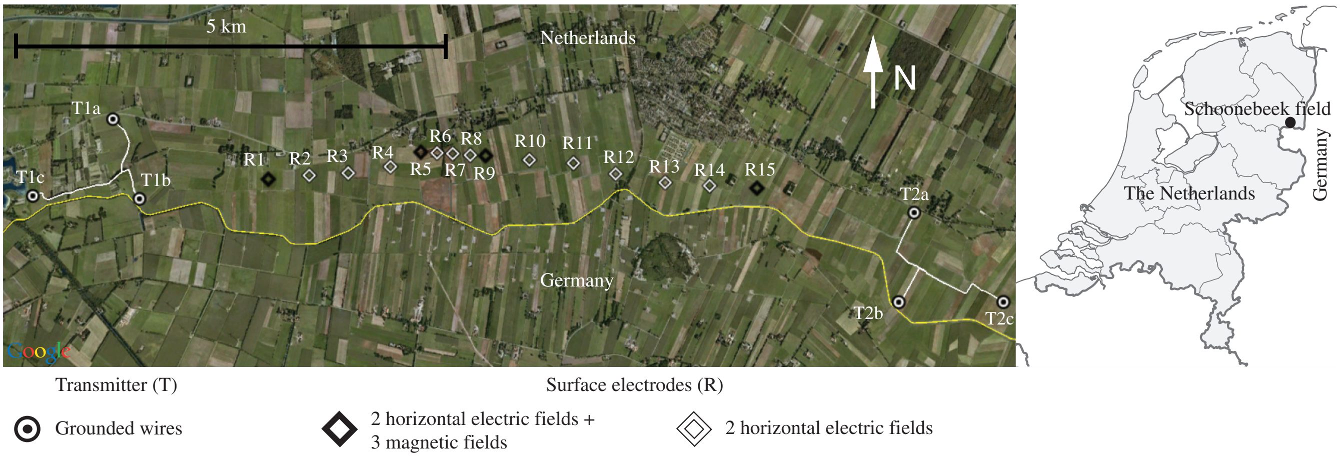

Figure 10. Location of field survey and detailed survey layout. Two transmitters are located west and east of the receiver line, respectively.

$\mu_i = 1.2$ and $p_c = 1.67$ and resistivity bounds of 2/3 Ωm and 10,000 Ωm were used, and frequencies greater than 10 Hz were neglected for the following 1D inversions (see the "1D inversion" section). We use 12 iterations to obtain our final inversion result.

The horizontal electric-field data were inverted for the anisotropic resistivity distribution using either a homogeneous half-space starting model or a starting model with a more complex near-surface resistivity distribution derived from recent well-log data.

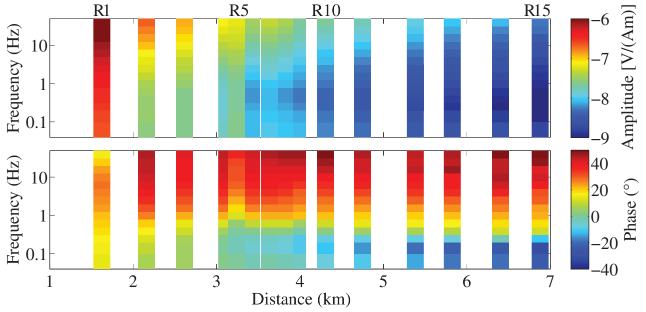

Figure 11. Response functions for component $T^{E_x}_{1,2}$ and for transmitter location 1 for all 15 receiver stations as a function of distance from source center and frequency.

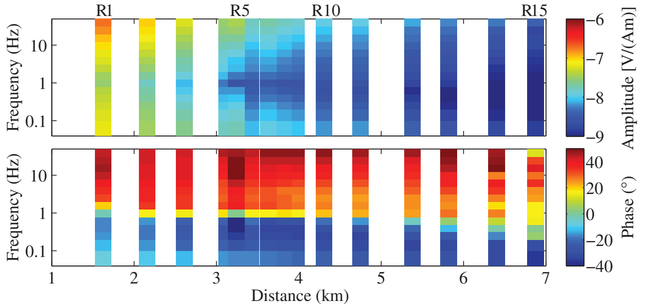

Figure 12. Response functions for component $T^{E_y}_{2,3}$ and for transmitter location 1 for all 15 receiver stations as a function of distance from source center and frequency.

Figure 13 shows three different inversion results obtained by changing the layer thicknesses in the starting model and by relaxing the regularization constraint at reservoir depth. Other inversion parameters were kept untouched. We obtain a smooth resistivity model with high vertical resistivity inside the reservoir (Figure 13a). Sensitivity to the horizontal resistivity in the reservoir is low and, thus, may explain why the inversion returns fairly low horizontal resistivity values. The reservoir is smoothed out to a vertical extent of approximately 200 m, much thicker than the expected extent of approximately 20 m. Because we are interested in deriving a suitable and realistic 1D model as the input for 3D inversion, we need to constrain our inversion to obtain a model closer to the real structure. One way of doing so is to use depth constraints imposed by seismic structure to regularize the CSEM inversion (Brown et al., 2012). This can be done by removing the regularization constraint (roughness penalty) at the expected depth of the reservoir (Myer et al., 2012). Figure 13b shows a resistivity model obtained after removing the smoothness constraint at the top of the reservoir at approximately 780 m. We obtain a reservoir with similar maximum vertical resistivity as before but exhibiting a sharp boundary at the depth level where regularization was removed. At the bottom of the reservoir, a sharp contrast could be introduced in the same way. However, we prefer the inversion to be less constrained by a fixed depth level and sharp contrasts in the model may cause artifacts in subsequent 3D inversion. Therefore, we introduce a fine layering of 2 m around the expected reservoir level, while keeping increasing layer thickness with depth elsewhere. Figure 13c shows that the vertical extent of the reservoir is much smaller now than for the previous models. In addition, the vertical resistivity of approximately 280 Ωm is much closer to values suggested by the resistivity logs. The final rms errors for all three models are given in the figure parts and are similar to each other.

Independent of the regularization and the chosen constraints, the transverse resistance, i.e., the integral of resistivity times layer thickness over the reservoir interval, should be better defined than resistivity and layer thickness individually and should be similar for all inversion models (Constable and Weiss, 2006; Key, 2012). We obtain the following values for the vertical transverse resistance of the reservoir: 6200 Ωm$^2$ for the smooth model from Figure 13a, integrating over a depth range from 800 to 1050 m, 5600 Ωm$^2$ for the model in Figure 13b (integration range 750–950 m), and 5400 Ωm$^2$ for the model in Figure 13c (integration range 750–900 m). The transverse resistance values are fairly similar but not identical. These results illustrate the ambiguity of the inversion together with the conclusions of Salako et al. (2015) that the best resolved parameter in CSEM is an estimate of bulk electrical resistivity for the reservoir.

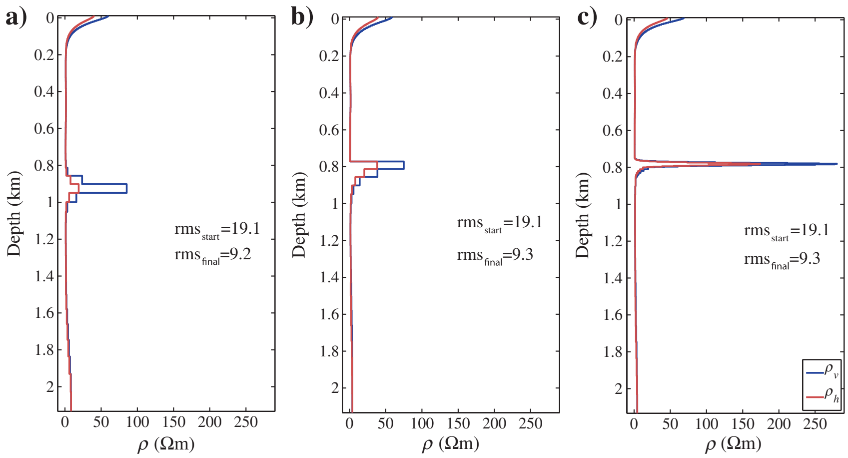

Figure 13. One-dimensional inversion results using (a) a coarse depth spacing with 83 layers of increasing thickness with depth, (b) the same depth intervals but freeing the regularization constraint at expected reservoir depth of 780 m, and (c) fine layering of 2 m around reservoir depth.

Because we have near-surface resistivity values from a shallow well log acquired prior to the CSEM survey near receiver R7 (see Figure 1), we also tested fixing the near surface and only allowing updates for the deeper layers. The resulting resistivity profile is depicted in Figure 14a.

Comparing this model to a synthetic model obtained solely from well-log information (see Figure 14b), we find that the reservoir is located at similar depths, and the resistivity variations above the reservoir follow a similar trend. Layers below the reservoir are not resolvable by our inversion due to limited penetration depth and the resistive nature of the reservoir and thus are not interpreted.

For our final model to be used for our 3D inversion, response functions from sources and all receivers were inverted jointly.

Misfits between synthetic and real data, as defined in equation 2 but without summing over frequency and space, are shown in Figure 15. It can be seen that the misfits improve over the entire frequency spectrum for both horizontal electric-field components. Receiver R1, R5, and R15 are not plotted here because they were not used in the inversion (see the discussion of these receivers above).

So far, we have treated the geology of the Schoonebeek area as being horizontally layered. Figure 16 highlights the depth of the base of the Bentheim sandstone at Schoonebeek, in which the reservoir is located. The horizon was picked from seismic images and clearly indicates complex fault structures and a dipping reservoir. The reservoir depth is shallower than 700 m in the center of our profile and increases to more than 800 m at the sides. Therefore, inverting each receiver separately may reveal a higher resolution per receiver position. In Figure 17, each receiver was inverted separately for transmitter location 1. The inversion indicates slightly increasing reservoir depths away from the center of the profile, which is in agreement with the regional geology (see Figure 16). Because the resistive reservoir extends far beyond the acquisition layout and data from a source-receiver pair are mainly affected by the structures in between, anomalies from the reservoir get stronger with the increasing source-receiver distance as more of the anomalously resistive body enters the volume being sampled (Myer et al., 2012). This may explain that the reservoir resistivities seen by receivers R2 and R4 closest to the source are lower than those of the other receivers (Figure 17).

As a final 1D inversion test, we investigate the dependency of inversion results on source polarization. Response functions computed directly by applying equation B-3, assuming zero transmitter current on one source electrode, correspond to polarizations of 30°, 90°, 150°, 210°, 270°, and 330°. Inversions shown in Figures 13, 14, and 17 used three of these polarizations simultaneously (30°, 330(−30)°, and 270°, corresponding to $\mathbf{T}_{1,2}$, $\mathbf{T}_{1,3}$, and $\mathbf{T}_{2,3}$ according to equation B-3). Data for other source polarizations can be generated by numeric source rotation (Streich et al., 2013). Figure 18 shows inversion results for 18 different source polarizations, inverting for a single polarization at a time. This shows that the "native" polarizations of 30°, 90°, and 150° provide poorer images of the reservoir than many of the other polarizations tested. The quality of the inversion results may thus be enhanced by choosing a different set of polarizations. Start and final rms errors give a further indication about the quality of the inversion results. For most of the 18 polarizations, the lowest errors correspond with polarizations in which the reservoir is best resolved. For further inversions, we use polarizations of 20°, 80°, and 140°.

For the 1D inversion, we can conclude that the reservoir can be clearly resolved. Modifying the roughness constraint to allow for jumps in resistivity or introducing small layering around the reservoir location may add structure to the inversion model. Changes of the reservoir depth along the profile agree with known geology. However, because not every source-receiver pair images the reser-

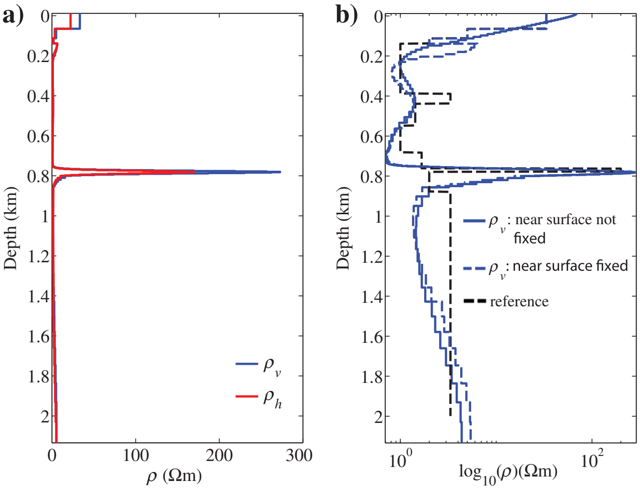

Figure 14. (a) One-dimensional subsurface resistivity profile with fixed near-surface layers and (b) comparison of 1D subsurface resistivity profile with and without fixed near-surface layers to 1D subsurface resistivity profile obtained from well-log data. For better visibility, the resistivity is plotted in logarithmic scale.

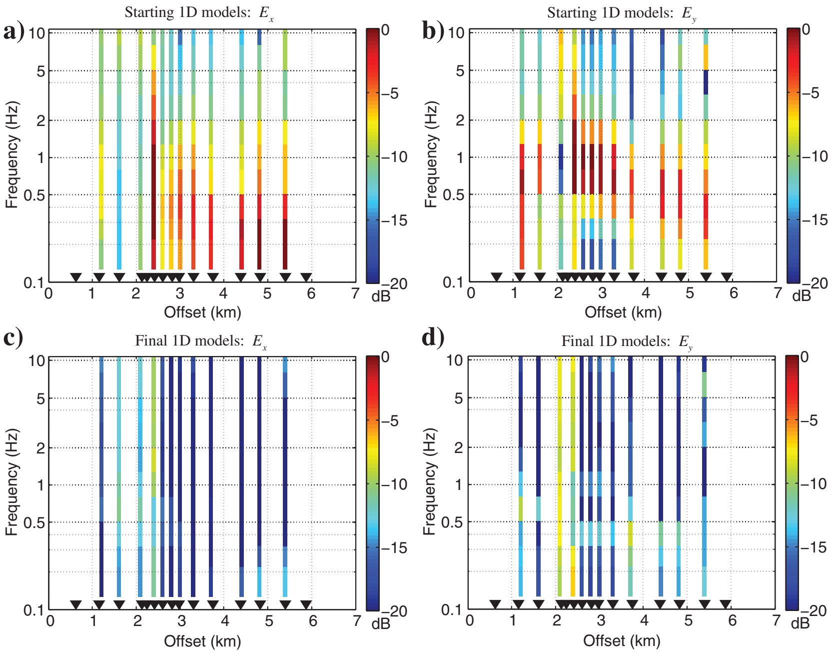

Figure 15. Data misfits for transmitter 1 before (a) and after (c) inversion for $E_x$ for source polarization 30° and misfits before (b) and after (d) inversion for $E_y$ for source polarization 270°.

voir clearly, 3D models obtained by interpolating individual-receiver inversion results tend to contain a more blurry image of the reservoir. This was found to be disadvantageous for subsequent 3D inversion. Therefore, we used the 1D subsurface resistivity profile with fixed near-surface layers obtained from multireceiver inversion with joint sources (Figure 14) as the input starting model for our 3D inversion.

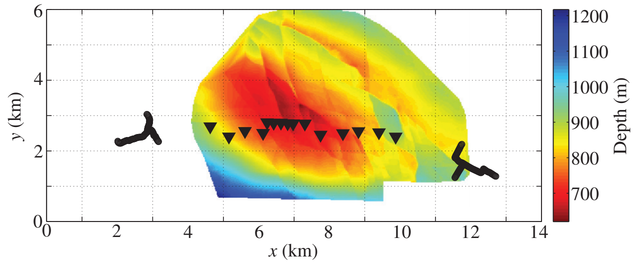

Figure 16. Depth of the base of the Bentheim sandstone. Black triangles and lines indicate the survey geometry.

## 3D inversion

Resistivity heterogeneities inside the reservoir due to steam injection are expected to exhibit rather complex 3D patterns. Overall, steam injection is likely to reduce reservoir resistivity (Mansure et al., 1993; Butler and Knight, 1995). However, reservoir simulation data suggest (Streich, 2016) that areas of increasing as well as decreasing resistivity are expected at Schoonebeek due to simultaneously ongoing processes of different magnitudes, lengths, and timescales. Temperature increase, gradual condensation of steam, displacement of highly resistive oil, as well as the reduction of salt concentration due to the mixing of steam with saline water are some of the processes that may lead to compartmentalization of the reservoir with different zones showing increasing and decreasing resistivity, respectively (Tøndel et al., 2014). Thus, 3D inversion of the EM data is needed. Because 3D inversion of our sparse data set is strongly under-determined, and our 3D inversion uses a quasi-Newton algorithm (contrary to Gauss-Newton for the 1D inversion), choosing an appropriate starting model is important. We therefore study the influence of different starting models to the inversion result. At first, we use our best 1D inversion model from Figure 14a, ignoring the known dip of the reservoir (Figure 19a). As a second attempt, we use a 2D model built by extracting the reservoir topography underneath the receiver line from the horizon shown in Figure 16. The top 580 m is left unchanged from the 1D model. At depths below 580 m, resistivities are defined by shifting the 1D resistivity column vertically such that the resistivity maximum coincides with the depth of the picked horizon (Figure 20a). Third, we use a 3D model in which the 1D resistivity column is shifted vertically, as for the 2D model, but this time the depths of the entire Bentheim sandstone horizon was used, and the model was modified from the 1D column at depths below 400 m (Figure 21a). The applied starting model is used as a reference model for the regularization, i.e., the difference of the model vector $\mathbf{m}$ from an a-priori model $\mathbf{m_0}$ is considered, resulting in a regularization based on the deviation from the starting model. For our real data, we applied the same parameters that were used for the synthetic inversion studies.

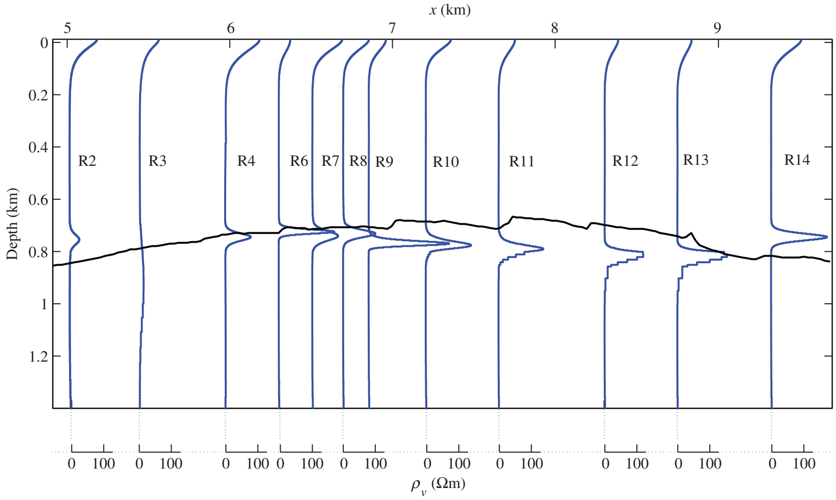

Figure 17. One-dimensional inversion results for transmitter location 1, inverting each receiver separately. For reference, the black line indicates the depth of the base of the Bentheim sandstone as shown in Figure 16.

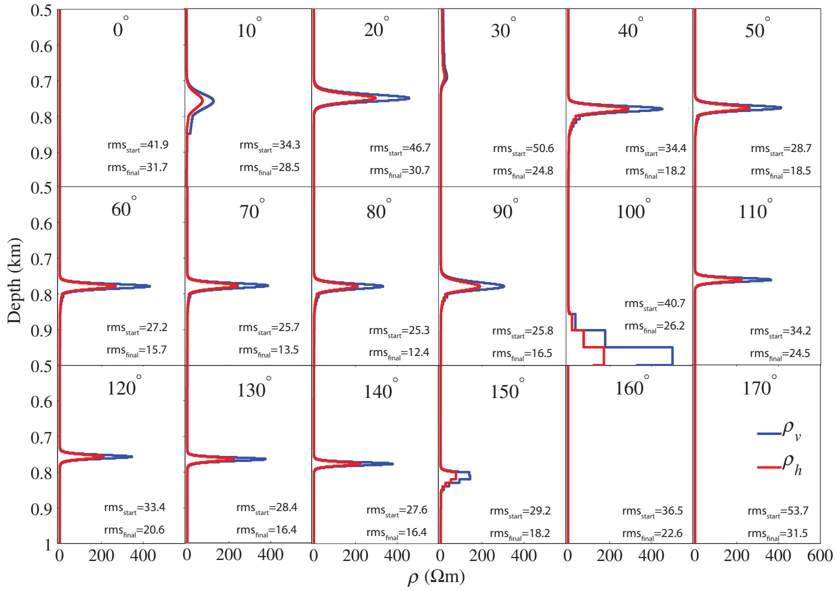

Figure 18. Dependence of the 1D inversion result on source polarization for the horizontal electric-field components $E_x$ and $E_y$ and for transmitter location 1 using all receiver stations. Start and final rms errors are given for each polarization.

Figure 19 shows 3D inversion results using the 1D starting model. The starting and final resistivity models as well as the resistivity updates expressed as $\rho_{\mathrm{final}}/\rho_{\mathrm{start}}$ are plotted in logarithmic scale. Assuming an average or typical resistivity for the reservoir, the resistivity updates may give an indication about the lateral variations within this reservoir. Trajectories of one steam injection (red) and two adjacent oil production (blue) wells are included for reference. Steam injection and production through these wells are expected to locally affect reservoir resistivities. There are many more wells in the field though, and the impact of the casings on our data certainly needs to be assessed further.

Due to the high resistivity of the reservoir, model updates are concentrated inside the reservoir where the sensitivity of the measurements is expected to be the highest (see Figure 4). Figure 19 indicates that reservoir resistivity is increased especially between $x = 5$–7 and 8–10 km.

For the 2D starting model (Figure 20), model updates focus on the reservoir and show a general increase in reservoir resistivity along the entire receiver array but most strongly at the dipping flanks of the reservoir. For the 3D starting model (Figure 21), the inversion result shows a strong resistivity increase especially east of the production and injection wells. The inversion result from the 3D starting model (Figure 21) is most consistent with our expectations. The model updates in Figure 21c suggest a gap in the resistor near the well where intermittent water injection during decades of production and recent steam injection took place. This has most likely created a more conductive region around the injection well. Surface measurements alone, though, are not capable of distinguishing between the types of the injected fluid. Thus, supplementary borehole-to-surface measurements (Wirianto et al., 2010), measurements of the vertical electric field and/or high-resolution seismics (Hornman and Forgues, 2013; Michou et al., 2013) are required to image the reservoir and its fluid content in more detail.

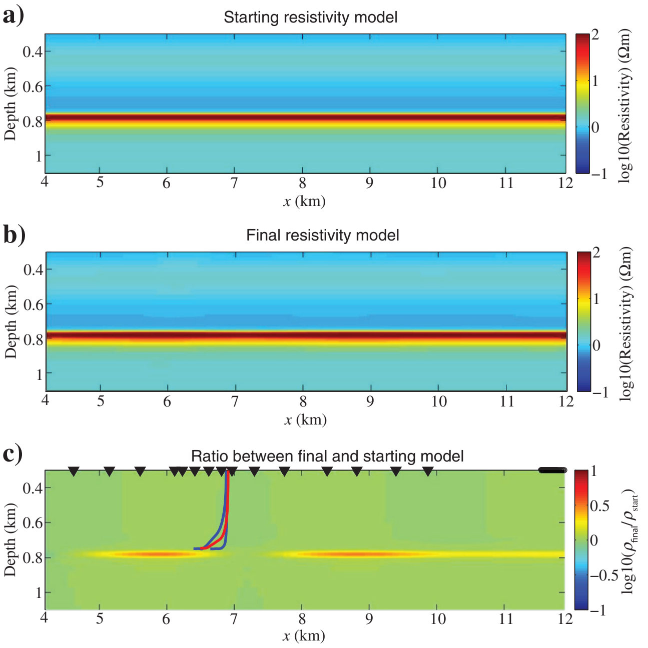

Figure 19. Depth sections at $y = 3$ km (see Figure 1) through (a) 1D starting model derived from 1D inversion results, (b) resistivity model after 3D inversion of $E_x$ and $E_y$ data, and (c) resistivity updates . The red and blue lines are trajectories of steam injection and production wells projected into the section. The black dots and triangles indicate source and receiver locations, respectively.

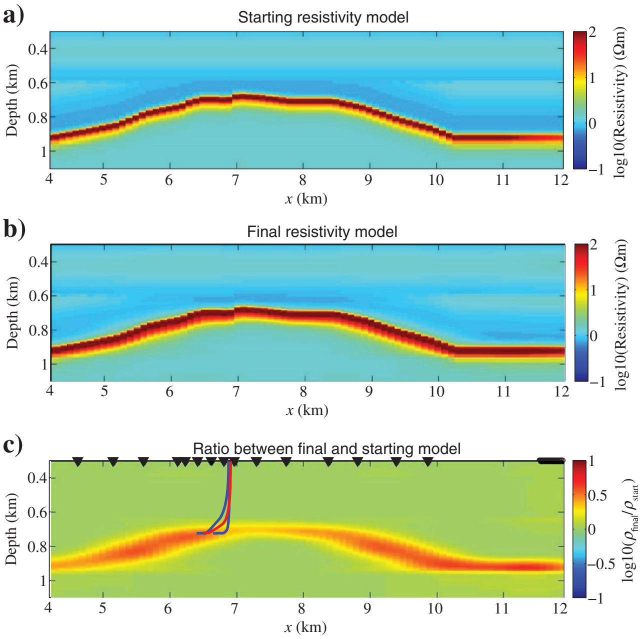

Figure 20. Depth sections at $y = 3$ km through (a) 2D starting model derived from 1D inversion results and the horizon shown in Figure 16, and (b) resistivity model after 3D inversion of $E_x$ and $E_y$ data. Resistivity updates are shown in (c). The projected well trajectories are plotted in blue (production wells) and red (injection well).

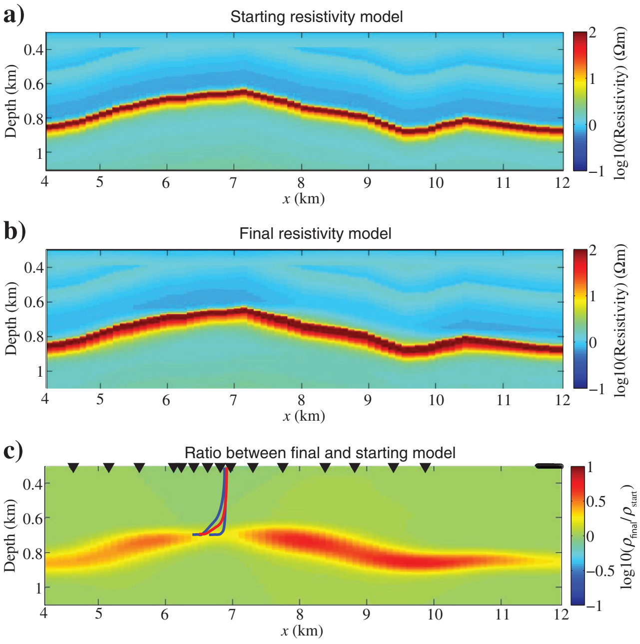

Figure 21. Depth sections at $y = 3$ km through (a) 3D starting model, and (b) resistivity model after 3D inversion of $E_x$ and $E_y$ data. Resistivity updates are shown in (c). The projected well trajectories are plotted in blue (production wells) and red (injection well).

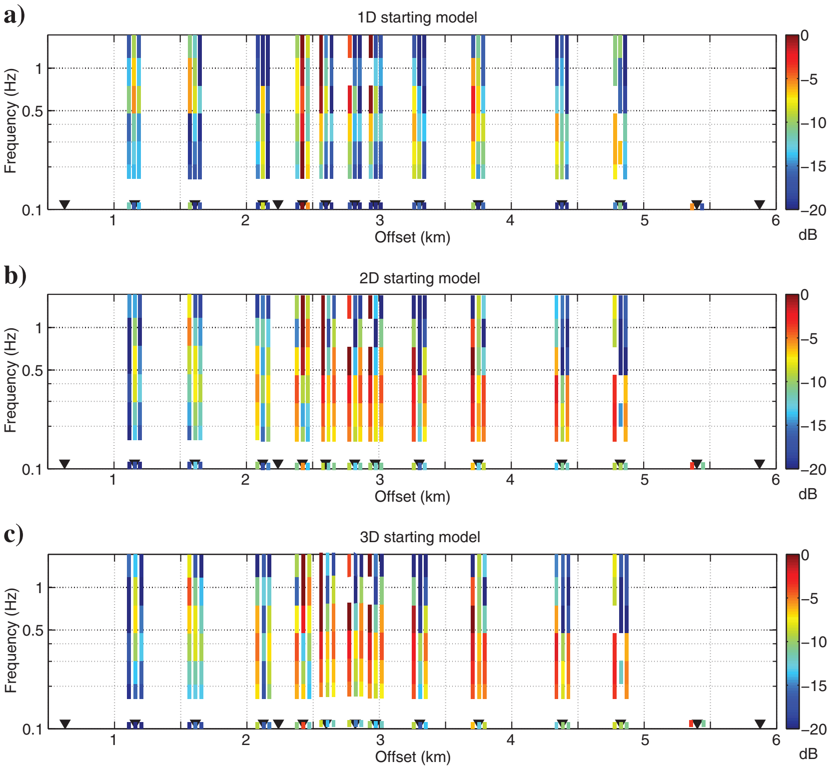

Figure 22. Data misfits for transmitter 1 before inversion for $E_y$ and for all three source polarizations using a (a) 1D, (b) 2D, and (c) 3D starting model.

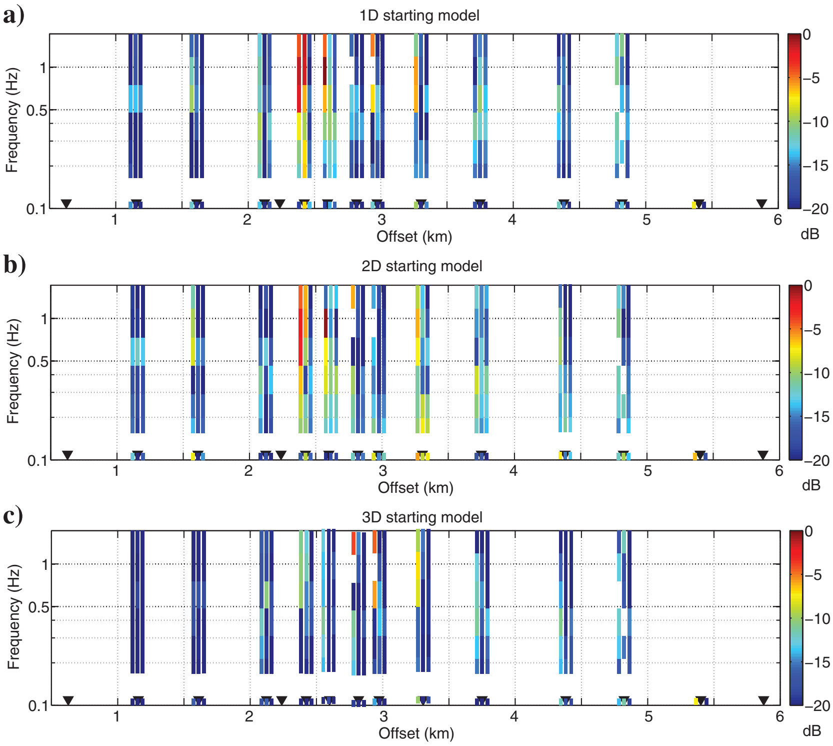

Figure 23. Data misfits for transmitter 1 after inversion for $E_y$ and for all three source polarizations using a (a) 1D, (b) 2D, and (c) 3D starting model.

The misfit is measured by using the least-square functional as described in equation 4. Figures 22 and 23 show the starting and final data misfits for the horizontal electric-field components $E_y$ and for all three inversion scenarios. Although the starting data misfits between starting model and data are higher for the more complex 2D and 3D models (see Figure 22), the final misfit values for the 3D starting model are consistently lower, indicating a better data fit for all receivers (see Figure 23). The development of rms values throughout the inversions for each starting model is depicted in Figure 24. Again, using a more complex starting model results in a higher starting misfit but leads to better overall data fitting and lower final data misfits in the case of the 3D starting model. The rms values are significantly reduced compared with those obtained from 1D inversion, but we do not achieve ideal rms values of 1. This may indicate that we have somewhat overestimated the S/Ns in our data. Further iterations of these inversions (not shown) did not reduce the rms values significantly, while introducing structure we do not consider geologically meaningful.

Because we are interested in lateral resistivity variations inside the reservoir, we show in Figure 25 depth slices through the reservoir. The resistivity structure found within the resistive reservoir is similar for the more complex starting models (Figure 25b and 25c) and shows highly resistive zones between $x = 4$–6 km and 10–12 km close to transmitter 2. Using a simple 1D starting model instead results in high-resistivity zones closer to the center of the array which are wider in the $y$-direction than the region that should be resolvable according to our sensitivity analysis (see Figure 4).

Because our array is sparse and only 2D, the 3D inversion is highly influenced by the choice of starting models. The differences of the inversion results due to the complexity of the starting model indicate that inaccurate depth information is likely to be compensated by adapting the resistivity inside the reservoir. As Constable et al. (2014) states, we confirm that a single model cannot be considered as “preferred,” but multiple models together may provide a good understanding of the information contained in the data. However, acquisition imprints from source and receiver distributions and the (so-far) disregarded impact of steel well casings and pipelines limit the resolution capability of the inversion, apparently more so than suggested by our synthetic studies. This can likely be attributed to a more complex structure of the true subsurface. Indications of small-scale resistivity variations near the steam injection well are not visible in the inversion results in Figures 19–25. Doubtlessly,

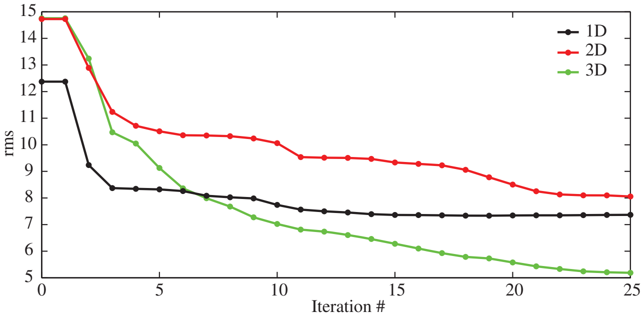

Figure 24. Development of the rms values for the three starting models.

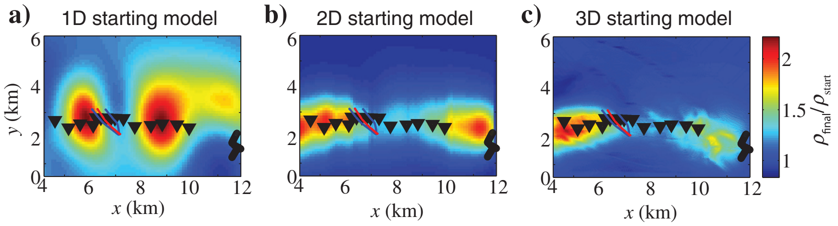

Figure 25. Map view of resistivity updates done by 3D inversion from (a) 1D, (b) 2D, and (c) 3D starting model, extracted at the depths in which starting resistivity is maximal, representing a layer of variable depth for the 2D and 3D starting models. Black triangles and lines indicate the survey geometry, and the red and blue lines indicate the well trajectories.

denser sources and receivers with better areal coverage will better constrain the background resistivity, thereby providing a clearer and more accurate image of the reservoir. Nevertheless, the results give an indication of resistivity variations inside the reservoir. Incorporating seismic data acquired at the site in the EM data may reduce the uncertainty in our interpretation (MacGregor et al., 2012).

One complication that has not been considered in this study, but needs to be considered in future further interpretation of these data, is the effect of steel well casings and pipelines on the data (Kong et al., 2009; Swidinsky et al., 2013; Commer et al., 2015; Patzer et al., 2017). We observed a signal-enhancing effect on receiver R5 where a steel-cased borehole is nearby. Commer et al. (2015) include highly conductive steel infrastructure in their earth modeling algorithms and confirm our observations that these casings change the signal distribution. Swidinsky et al. (2013) show the influence of steel borehole casings in the vicinity of a CSEM system and conclude that boreholes should either be positioned broadside with respect to the CSEM array or drilled at least 200 m away from the CSEM array to minimize the casing effects, which is conform to our observations.

## CONCLUSION

Our modeling study on survey geometry, resolution analysis, and depth penetration using cumulative sensitivity show that small resistive anomalies can be recognized but their size and resistivity are difficult to recover. However, complex structures cannot be resolved when assuming real-data uncertainties or noise conditions.

We could show that the highly resistive Schoonebeek reservoir can be clearly identified using a simple line survey geometry and horizontal electric-field data. From the multiple 1D and 3D inversions carried out, we also find indications of resistivity variation within the reservoir. However, the small-scale resistivity structure that may occur due to steam injection cannot be resolved using this data set alone.

Unconstrained 1D inversion can in general recover the correct reservoir depth. The introduction of fine layering around the predicted reservoir depth resulted in a geologically plausible 1D model that could be used as input for 3D inversion. Lateral variations and small resistive or conductive bodies inside the reservoir, however, could not be resolved as was already anticipated from the synthetic studies.

Interpretation of the 3D structure in the obtained inversion models is difficult without further constraints. Most likely, the results show actual reservoir structure with an imprint of acquisition geometry. Unaccounted features from the metal infrastructure may have further limited effects.

To be able to detect small-scale resistivity variations or time-lapse changes induced due to hydrocarbon production or steam injection, we would require better EM data coverage and more accurate knowledge of the background resistivity model. Additional information can be gathered from well-logs, geologic information, different EM data such as the vertical electric field $E_z$ or from other geophysical data (e.g., seismic). Closer integration of the EM data with seismic data acquired at the site may further reduce the uncertainty in our interpretation.

## ACKNOWLEDGMENTS

We would like to thank R. Klose and S. Rettig from the Helmholtz Centre Potsdam, GFZ German Research Centre for Geosciences for their help in the field, particularly for operating the CSEM source. Furthermore, we are very grateful to the Geophysical Instrument Pool Potsdam (GIPP) for providing some of the EM receiver equipment. In addition, we would like to thank all the TU Delft staff and students who helped us with the field work, the farmers for letting us access their property, and NAM (Nederlandse Aardolie Maatschappij BV) for permitting and surveying support, and for allowing us to publish information on the Schoonebeek reservoir.

## APPENDIX A

## TRANSMITTER SPECIFICATIONS

The overall configuration of the transmitter can be seen in Figure A-1. The CSEM transmitter developed by Metronix GmbH and the German Research Centre for Geosciences (GFZ) is powered by a 400 V generator that supplies three-phase 50 Hz alternating currents. The currents are fed into a programmable signal generator. Custom waveforms can be designed to spread the transmitted energy across a band of discrete frequencies in a more even manner than the linear amplitude decrease of the traditional square wave (Mittet and Schaug-Pettersen, 2008; Myer et al., 2011). During most of our survey, we still use square-wave signals with different source base frequencies because this proved to be best suited for elevating signal levels above ambient noise levels in the survey area.

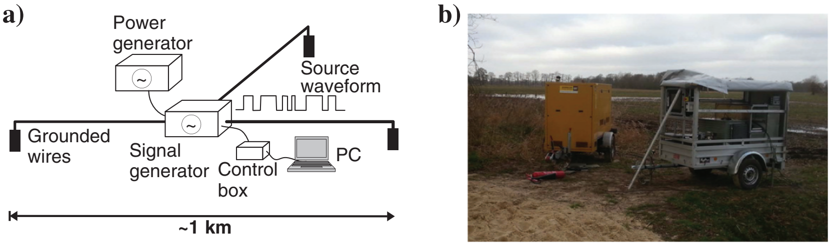

Figure A-1. (a) Sketch of the CSEM source (after Streich et al., 2010). (b) Land CSEM transmitter; 400 V power generator (yellow) that supplies three-phase, 50 Hz AC current. Inside the white trailer a high-power, high voltage programmable signal generator creates the desired waveform.

The overall source strength is determined by the length of the grounded electric source wires (approximately 1 km for our survey; see Figure 1) and the current amplitudes that can reach up to 40 A. In Schoonebeek, the electrode contact resistances were reduced such that maximum currents of approximately 35 A were achieved.

The three-phase CSEM transmitter can easily generate multipolarization signals. The three currents fed into the three grounded electrodes are phase shifted to each other by 120°. The current $I_k$ on electrode $k \in \{1, 2, 3\}$ can be written as (Streich et al., 2013)

$$I_k = I_0 \cos[(k-1) * 120^\circ + \phi], \tag{A-1}$$

where $I_0$ is the time-dependent source waveform and $\phi$ is the polarization angle. By electronically adjusting the polarization angle, multipolarization fields are generated without redeploying the transmitter. Transmitter cable locations are recorded by GPS, and the exact source geometry is included into forward calculation and data inversion (Streich et al., 2011).

## APPENDIX B

## RESPONSE FUNCTION CALCULATION

The electric field $\mathbf{E}$ in the frequency domain at position $\mathbf{r}$ is a superposition of the fields due to each part of the source and can be rewritten in terms of response functions according to (Streich et al., 2013)

$$\mathbf{E}(\mathbf{r}) = \sum_{k=1}^{3} I_k i\omega\mu_0 \int_{L_k} \bar{\bar{\mathbf{G}}}^{EJ}(\mathbf{r}|\mathbf{r}') \cdot d\mathbf{l}' = \sum_{k=1}^{3} I_k \mathbf{T}_k^{\mathbf{E}}, \tag{B-1}$$

where $i = \sqrt{-1}$, $\omega$ is the angular frequency and $\mu_0$ is the free-space magnetic permeability. The integration is carried out over the individual length of the grounded wires $L_k$, and $\bar{\bar{\mathbf{G}}}^{EJ}$ is the Green's tensor for electric fields due to electric dipole sources and $\mathbf{T}_k^{\mathbf{E}}$ are the response functions for a given source geometry that are independent of the current waveform. They contain information on the subsurface resistivity but cannot be measured directly. Convolving these response functions with the three source currents and superposing them B-1 leads to the fields that are recorded. From equation A-1, it follows that the three source currents are linearly dependent with

$$\sum_{k=1}^{3} I_k = 0. \tag{B-2}$$

Therefore, the response functions $\mathbf{T}_k^{\mathbf{E}}$ cannot be determined separately from each other and one of the currents has to be eliminated; in case, $I_3$ is eliminated, we get

$$\begin{aligned} \mathbf{E}(\mathbf{r}) &= I_1(\mathbf{T}_1^{\mathbf{E}} - \mathbf{T}_3^{\mathbf{E}}) + I_2(\mathbf{T}_2^{\mathbf{E}} - \mathbf{T}_3^{\mathbf{E}}) \\ &= I_1\mathbf{T}_{1,3}^{\mathbf{E}} + I_2\mathbf{T}_{2,3}^{\mathbf{E}}, \end{aligned} \tag{B-3}$$

resulting in bivariate CSEM response functions $\mathbf{T}_{1,3}^{\mathbf{E}}$ and $\mathbf{T}_{2,3}^{\mathbf{E}}$. The relation between the horizontal electric-field data and the two source currents can be expressed in matrix form as

$$\begin{pmatrix} E_x \\ E_y \end{pmatrix} = \begin{pmatrix} T_{1,3}^{E_x} & T_{2,3}^{E_x} \\ T_{1,3}^{E_y} & T_{2,3}^{E_y} \end{pmatrix} \begin{pmatrix} I_1 \\ I_2 \end{pmatrix}, \tag{B-4}$$

where the response functions are determined by a robust weighted least-squares averaging over data from different source currents and source fundamental frequencies as described in Streich et al. (2013).

## REFERENCES

Brown, V., G. M. Hoversten, and K. Key, 2012, Seismically regularized controlled-source electromagnetic inversion: Geophysics, **77**, no. 1, E57–E65, doi: 10.1190/geo2011-0081.1.

Butler, D. B., and R. J. Knight, 1995, The effect of steam quality on the electrical behavior of steam-flooded sands: A laboratory study: Geophysics, **60**, 998–1006, doi: 10.1190/1.1443864.

Byrd, R. H., P. Lu, J. Nocedal, and C. Zhu, 1995, A limited memory algorithm for bound constrained optimization: SIAM Journal on Scientific Computing, **16**, 1190–1208, doi: 10.1137/0916069.

Chave, A. D., and D. J. Thomson, 1989, Some comments on magnetotelluric response function estimation: Journal of Geophysics Research, **94**, 215–214.

Commer, M., G. M. Hoversten, and E. S. Um, 2015, Transient-electromagnetic finite- difference time-domain earth modeling over steel infrastructure: Geophysics, **80**, no. 2, E147–E162, doi: 10.1190/geo2014-0324.1.

Commer, M., and G. A. Newman, 2008, New advances in three-dimensional controlled-source electromagnetic inversion: Geophysical Journal International, **172**, 513–535, doi: 10.1111/j.1365-246X.2007.03663.x.

Constable, S., 2010, Ten years of marine CSEM for hydrocarbon exploration: Geophysics, **75**, no. 5, 75A67–75A81, doi: 10.1190/1.3483451.

Constable, S., A. Orange, and K. Key, 2014, And the geophysicist replied: “Which model do you want?”: Geophysics, **80**, no. 3, E197–E212, doi: 10.1190/geo2014-0381.1.

Constable, S., and C. J. Weiss, 2006, Mapping thin resistors and hydrocarbons with marine EM methods: Insights from 1D modeling: Geophysics, **71**, no. 2, G43–G51, doi: 10.1190/1.2187748.

Constable, S. C., R. L. Parker, and C. G. Constable, 1987, Occam's inversion: a practical algorithm for generating smooth models from electromagnetic sounding data: Geophysics, **52**, 289–300, doi: 10.1190/1.1442303.

Darnet, M., M. C. K. Choo, R. Plessix, M. L. Rosenquist, K. Yip-Cheong, E. Sims, and J. W. K. Voon, 2007, Detecting hydrocarbon reservoirs from CSEM data in complex settings: Application to deepwater Sabah, Malaysia: Geophysics, **72**, no. 2, WA97–WA103, doi: 10.1190/1.2435201.

deGroot Hedlin, C., and S. Constable, 1990, Occam's inversion to generate smooth, two-dimensional models from magnetotelluric data: Geophysics, **55**, 1613–1624, doi: 10.1190/1.1442813.

Dell'Aversana, P., S. Colombo, B. Ciurlo, J. Leutscher, and J. Seldal, 2012, CSEM data interpretation constrained by seismic and gravity data: An application in a complex geological setting: First Break, **30**, 43–52.

Egbert, G. D., and J. R. Booker, 1986, Robust estimation of geomagnetic transfer functions: Geophysical Journal International, **87**, 173–194, doi: 10.1111/j.1365-246X.1986.tb04552.x.

Ellingsrud, S., T. Eidesmo, S. Johansen, M. Sinha, L. MacGregor, and S. Constable, 2002, Remote sensing of hydrocarbon layers by seabed logging (SBL): Results from a cruise offshore Angola: The Leading Edge, **21**, 972–982, doi: 10.1190/1.1518433.

Fanavoll, S., P. T. Gabrielsen, and S. Ellingsrud, 2014, CSEM as a tool for better exploration decisions: Case studies from the Barents Sea, Norwegian Continental Shelf: Interpretation, **2**, no. 3, SH55–SH66, doi: 10.1190/INT-2013-0171.1.

Farquharson, C. G., and D. W. Oldenburg, 1998, Non-linear inversion using general measures of data misfit and model structure: Geophysical Journal International, **134**, 213–227, doi: 10.1046/j.1365-246x.1998.00555x.

Grayver, A., R. Streich, and O. Ritter, 2013, Three-dimensional parallel distributed inversion of CSEM data using a direct forward solver: Geophysical Journal International, **193**, 1432–1446, doi: 10.1093/gji/ggt055.

Grayver, A. V., R. Streich, and O. Ritter, 2014, 3D inversion and resolution analysis of land-based CSEM data from the Ketzin $CO_2$ storage formation: Geophysics, **79**, no. 2, E101–E114, doi: 10.1190/geo2013-0184.1.

Haber, E., U. M. Ascher, and D. Oldenburg, 2000, On optimization techniques for solving nonlinear inverse problems: Inverse problems, **16**, 1263–1280, doi: 10.1088/0266-5611/16/5/309.

Hornman, K., and E. Forgues, 2013, Permanent reservoir monitoring with onshore surface seismic: Presented at the Second EAGE Workshop on Permanent Reservoir Monitoring 2013-Current and Future Trends.

Key, K., 2009, 1D inversion of multicomponent, multifrequency marine CSEM data: Methodology and synthetic studies for resolving thin resistive layers: Geophysics, **74**, no. 2, F9–F20, doi: 10.1190/1.3058434.

Key, K., 2012, Marine electromagnetic studies of seafloor resources and tectonics: Surveys in Geophysics, **33**, 135–167, doi: 10.1007/s10712-011-9139-x.

Klose, R., G. Schmidt, O. Ritter, and G. Dawes, 2011, What is SPAM four for?: Protokollüber das 24. Schmucker-Weidelt-Kolloquium für Elektromagnetische Tiefenforschung, 24. Schmucker-Weidelt-Kolloquium für Elektromagnetische Tiefenforschung (Neustadt a. d. Weinstraße 2011), 127–134.

Kong, F. N., F. Roth, P. A. Olsen, and S. O. Stalheim, 2009, Casing effects in the sea-to-borehole electromagnetic method: Geophysics, no. 2, **74**, F77–F87, doi: 10.1190/1.3173807.

Li, Y., and D. W. Oldenburg, 1998, 3-D inversion of gravity data: Geophysics, **63**, 109–119, doi: 10.1190/1.1444302.

MacGregor, L., S. Bouchrara, J. Tomlinson, U. Strecker, J. Fan, X. Ran, and G. Yu, 2012, Integrated analysis of CSEM, seismic and well log data for prospect appraisal: A case study from West Africa: First Break, **30**, 77–82.

Mansure, A. J., R. F. Meldau, and H. V. Weyland, 1993, Field examples of electrical resistivity changes during steamflooding: SPE Formation Evaluation, **8**, 57–64, doi: 10.2118/20539-PA.

Michou, L., T. Coléou, and Y. Lafet, 2013, 4D seismic inversion on continuous land seismic reservoir monitoring of thermal EOR: 75th Annual International Conference and Exhibition, EAGE, Extended Abstracts, doi: 10.3997/2214-4609.20130427.

Mittet, R., and T. Schaug-Pettersen, 2008, Shaping optimal transmitter waveforms for marine CSEM surveys: Geophysics, **73**, no. 3, F97–F104, doi: 10.1190/1.2898410.

Mulder, W., 2006, A multigrid solver for 3D electromagnetic diffusion: Geophysical Prospecting, **54**, 633–649, doi: 10.1111/j.1365-2478.2006.00558.x.

Myer, D., S. Constable, and K. Key, 2011, Broad-band waveforms and robust processing for marine CSEM surveys: Geophysical Journal International, **184**, 689–698, doi: 10.1111/j.1365-246X.2010.04887.x.

Myer, D., S. Constable, K. Key, M. E. Glinsky, and G. Liu, 2012, Marine CSEM of the Scarborough gas field, Part 1: Experimental design and data uncertainty: Geophysics, **77**, no. 4, E281–E299, doi: 10.1190/geo2011-0380.1.

Newman, G. A., 2014, A review of high-performance computational strategies for modeling and imaging of electromagnetic induction data: Surveys in Geophysics, **35**, 85–100, doi: 10.1007/s10712-013-9260-0.

Oldenburg, D. W., E. Haber, and R. Shekhtman, 2013, Three dimensional inversion of multisource time domain electromagnetic data: Geophysics, **78**, no. 1, E47–E57, doi: 10.1190/geo2012-0131.1.

Patzer, C., K. Tietze, and O. Ritter, 2017, Steel-cased wells in 3-D controlled source EM modelling: Geophysical Journal International, **209**, 813–826, doi: 10.1093/gji/ggx049.

Plessix, R. E., M. Darnet, and W. A. Mulder, 2007, An approach for 3D multisource, multifrequency CSEM modeling: Geophysics, **72**, no. 5, SM177–SM184, doi: 10.1190/1.2744234.

Plessix, R. E., and W. A. Mulder, 2008, Resistivity imaging with controlled-source electro-magnetic data: Depth and data weighting: Inverse Problems, **24**, 034012, doi: 10.1088/0266-5611/24/3/034012.

Ritter, O., A. Junge, and G. J. Dawes, 1998, New equipment and processing for magnetotelluric remote reference observations: Geophysical Journal International, **132**, 535–548, doi: 10.1046/j.1365-246X.1998.00440.x.

Rondeel, H., D. Batjes, and W. Nieuwenhuijs, 1996, Geology of gas and oil under the Netherlands: Springer Netherlands.

Salako, O., C. MacBeth, and L. MacGregor, 2015, Potential applications of time-lapse CSEM to reservoir monitoring: First Break, **33**, 35–46, doi: 10.3997/1365-2397.2014025.

Schwarzbach, C., and E. Haber, 2013, Finite element based inversion for time-harmonic electromagnetic problems: Geophysical Journal International, **193**, 615–634, doi: 10.1093/gji/ggt006.

Streich, R., 2016, Controlled-source electromagnetic approaches for hydrocarbon exploration and monitoring on land: Surveys in Geophysics, **37**, 47–80, doi: 10.1007/s10712-015-9336-0.

Streich, R., and M. Becken, 2011, Sensitivity of controlled-source electromagnetic fields in planarly layered media: Geophysical Journal International, **187**, 705–728, doi: 10.1111/j.1365-246X.2011.05203.x.

Streich, R., M. Becken, U. Matzander, and O. Ritter, 2011, Strategies for land-based controlled-source electromagnetic surveying in high-noise regions: The Leading Edge, **30**, 1174–1181, doi: 10.1190/1.3657078.

Streich, R., M. Becken, and O. Ritter, 2010, Imaging of $CO_2$ storage sites, geothermal reservoirs, and gas shales using controlled-source magnetotellurics: Modeling studies: Chemie der Erde — Geochemistry, **70**, 63–75, doi: 10.1016/j.chemer.2010.05.004.

Streich, R., M. Becken, and O. Ritter, 2013, Robust processing of noisy land-based controlled-source electromagnetic data: Geophysics, **78**, no. 5, E237–E247, doi: 10.1190/geo2013-0026.1.

Swidinsky, A., R. N. Edwards, and M. Jegen, 2013, The marine controlled source electromagnetic response of a steel borehole casing: Applications for the NEPTUNE Canada gas hydrate observatory: Geophysical Prospecting, **61**, 842–856, doi: 10.1111/1365-2478.12007.

Tietze, K., O. Ritter, and P. Veeken, 2015, Controlled-source electromagnetic monitoring of reservoir oil saturation using a novel borehole-to-surface configuration: Geophysical Prospecting, **63**, 1468–1490, doi: 10.1111/1365-2478.12322.

Tøndel, R., H. Schütt, S. Dümmong, A. Ducrocq, R. Godfrey, D. LaBrecque, L. Nutt, A. Campbell, and R. Rufino, 2014, Reservoir monitoring of steam-assisted gravity drainage using borehole measurements: Geophysical Prospecting, **62**, 760–778, doi: 10.1111/1365-2478.12131.

Wirianto, M., W. A. Mulder, and E. C. Slob, 2010, A feasibility study of land CSEM reservoir monitoring in a complex 3-D model: Geophysical Journal International, **181**, 741–755, doi: 10.1111/j.1365-246X.2010.04544.x.

Zhdanov, M. S., M. Endo, L. H. Cox, M. Čuma, J. Linfoot, C. Anderson, N. Black, and A. V. Gribenko, 2014, Three-dimensional inversion of towed streamer electromagnetic data: Geophysical Prospecting, **62**, 552–572, doi: 10.1111/1365-2478.12097.